Entanglement analysis and experimental proposal for measuring Bell-type correlations in an injected optical parametric oscillator with structured light

L. G. S. Oliveira,[1,*] L. J. Pereira,[1,†] R. M. Pereira,[1,‡] G. B. Alves,[1,§] J. A. O. Huguenin,[1,2,‖] A. Z. Khoury,[1,¶] K. Dechoum,[1,#] and C. E. R. Souza[1,**]

[1]*Instituto de Física, Universidade Federal Fluminense, 24210-346 Niterói, RJ, Brazil*

[2]*Instituto de Ciências Exatas, Universidade Federal Fluminense, 27213-145 Volta Redonda, RJ, Brazil*

(Received 20 October 2023; accepted 4 March 2024; published 1 April 2024)

We study a type-II optical parametric oscillator under injection of laser beams with first-order Hermite-Gauss modes. We develop the equations describing the dynamics of this system in the Wigner representation of the density matrix. These equations are solved numerically and compared with the analytical solution in the nondepletion regime. We show that, when the injected beams are much less intense than the pumping beam, the system still exhibits quantum entanglement, which can be witnessed via Duan-Simon criterion and Bell inequalities. We also propose an experimental apparatus for measuring Bell inequalities. This system can generate spin-orbit hyperentangled states, and is thus a useful resource to quantum technology applications and fundamental physics.

DOI: 10.1103/PhysRevA.109.043701

I. INTRODUCTION

Entanglement is a useful property of quantum systems, characterized by nonclassical correlations between subsystems. It was first conceived by Schrödinger in his famous thought experiment [1] involving a cat in a peculiar state of being both dead and alive, and later explored by Einstein, Podolsky, and Rosen (EPR) [2]. The history of science teaches us that the problems and enigmas of entangled systems were little addressed until 1964 with the publication of the work of John S. Bell, which established a way of discriminating the results predicted by quantum mechanics with the results of classical physics, within the idea of local realism [3]. Entanglement is the fundamental cornerstone of quantum technology. Among all known quantum systems, light stands out as an exceptionally promising platform for studying and advancing quantum technologies, already proving its efficacy in long-distance communication systems and simulating complex phenomena [4].

In quantum optics, it is observed that light is a nonclassical physical system which, in some situations, presents entanglement and that can be studied in two domains: the domain of discrete variables (DV) and the domain of continuous variables (CV). In the DV domain, the discrete nature of the optical field is directly evidenced in the measurement process, where the counting of single photons or coincidences are a clear manifestation of the quantum nature of the field, while in the CV approach the focus is on the quadrature operators, where homodyne measurement is used to measure quadrature correlations and, in general, their joint probability distribution, through continuous quasi-probability functions. Considered the most traditional approach, this method has been routinely employed since Aspect *et al.*'s pioneering work in experimentally determining entanglement in systems with polarized photons via Bell inequalities [5,6]. Aspect *et al.*'s work paved the way for the development of quantum encryption and quantum simulation devices [7–9]. In the CV domain, optical fields are decomposed into amplitude and phase quadratures. Optical parametric oscillators (OPOs) play a crucial role as physical devices, producing entangled laser beams in the CV domain, with significant potential applications in implementing quantum information protocols [10–12], quantum metrology [13,14], and quantum computing [15]. In addition, in recent years substantial efforts have been dedicated to the understanding and control of OPO for complex quantum tasks, which require scalability of useful degrees of freedom for quantum computing [16–18]. However, within this sphere of OPO development, both polarization and transverse modes have been extensively utilized. Specifically, the dynamics of spin-orbit modes in type-II OPOs were theoretically investigated in order to explore hyperentanglement in CV [19], and experimentally demonstrated in Ref. [20]. More recently, it was observed experimentally the orbital angular momentum (OAM) symmetry of the beams converted by an injected OPO [21], an effect governed by the conditions of the optical cavities [22,23].

Achieving the violation of Bell inequalities in CV presents a formidable challenge with far-reaching implications for quantum technology. This intricate matter was originally explored in Refs. [24,25], and subsequently experimentally implemented by Thearly *et al.* [26]. Their work demonstrates the actualization of Bell inequalities violation in the CV domain. This breakthrough was accomplished through the

*lsoares@id.uff.br
†justinolp10@gmail.com
‡rodrigomp@id.uff.br
§gbie@id.uff.br
‖jose_huguenin@id.uff.br
¶azkhoury@id.uff.br
#kaleddechoum@id.uff.br
**carloseduardosouza@id.uff.br

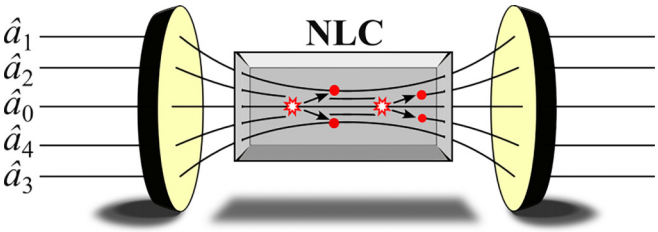

FIG. 1. A schematic diagram illustrating a triply resonant injected optical parametric oscillator with four decay channels, based simultaneously on two orthogonal polarization states and two orthogonal first-order Hermite-Gaussian modes.

utilization of two optical parametric oscillators in conjunction with a well-suited homodyne detection configuration.

In this paper, we investigate entanglement in a type-II OPO weakly injected by beams with first-order Hermite-Gauss modes. Analogously to the experimental setup developed by Thearly *et al.* [26], we will show that this system generates entangled beams that can violate the Bell inequalities. We present a quantum description of the OPO injected with spin-orbit beams via the Wigner representation. We analytically calculated, in a nondepletion regime, the amplitudes of the output fields, which will be taken as the basis for all correlations calculations, and compared the results with exact numerical calculations, which support and give confidence to the analytical results. The conditions predicted by the Duan-Simon and Bell criteria are obtained to demonstrate the entanglement. Finally, we propose an experimental apparatus for measuring the Bell inequalities in the CV domain in this system.

II. HAMILTONIAN AND STOCHASTIC EQUATIONS

Structured light has received special attention during the last years due to potential applications in quantum information and quantum communication. The spin-orbit modes are a special kind of structured light that combine polarization and transverse modes [27–29]. For example, spin-orbit modes can be defined by combining polarization and transverse modes as

$$E = A_1\psi_{HG10}\hat{e}_H + A_2\psi_{HG01}\hat{e}_H + A_3\psi_{HG10}\hat{e}_V + A_4\psi_{HG01}\hat{e}_V, \quad (1)$$

where A_i are complex amplitudes, ψ_{HG01} and ψ_{HG10} are the first-order Hermite-Gauss modes and $\hat{e}_H$ and $\hat{e}_V$ represent the linear horizontal and vertical polarization unit vectors, respectively. Note that depending on A_i, we can find a structure which cannot be factorized as a product between a spatial and a polarization structure, giving rise to nonseparable modes [27]. Here, we focus on the separable spin-orbit modes.

As illustrated in Fig. 1, the physical system considered here consists of an injected triply resonant type-II OPO for the *pumping beam* $\vec{E}_p$ and the seed beams: *signal* $\vec{E}_s$ and *idler* $\vec{E}_i$. The pumping beam is assumed to be prepared in the fundamental transverse mode ψ_{00} and the seed beams are restricted to the subspace of the first-order Hermite-Gauss modes $\{\psi_{HG10}, \psi_{HG01}\}$ [30]. Thus, we can write the equations describing the incident fields as

$$\begin{aligned}\vec{E}_p &= \mathcal{E}_0\psi_{00}\hat{\mathrm{e}}_H,\\ \vec{E}_s &= \mathrm{e}^{i\phi_1}\mathcal{E}_1\psi_{HG10}\hat{\mathrm{e}}_H + \mathrm{e}^{i\phi_2}\mathcal{E}_2\psi_{HG01}\hat{\mathrm{e}}_H,\\ \vec{E}_i &= \mathrm{e}^{i\phi_3}\mathcal{E}_3\psi_{HG10}\hat{\mathrm{e}}_V + \mathrm{e}^{i\phi_4}\mathcal{E}_4\psi_{HG01}\hat{\mathrm{e}}_V,\end{aligned} \quad (2)$$

where ψ_{HG01} and ψ_{HG10} are the first-order Hermite-Gauss (HG) modes and $\hat{\mathrm{e}}_H$ and $\hat{\mathrm{e}}_V$ represent the linear states of horizontal and vertical polarization, respectively. The amplitudes $\mathcal{E}_i$ and phases ϕ_i with $i = 1, ..., 4$ are parameters that can be adjusted to simulate seed beams as different first-order mode combinations. Note that signal and idler are assumed to be frequency degenerated, being distinguishable only through their polarization states. Note that for $E_1 = E_2$, $\phi_1 = 0$, $\phi_2 = +\pi/2$ and $E_3 = E_4$, $\phi_3 = 0$, $\phi_4 = -\pi/2$ we have the incidence of signal in the Laguerre-Gauss mode LG_{0+1}, and idler in the Laguerre-Gauss mode LG_{0-1}, both carrying orbital angular momentum (OAM). The general form of Eq. (1) enables us to explore the injection of different structures in the signal and idler beams described in the first-order subspace of separable spin-orbit modes. For simplicity and without loss of generality, we will study the injection of HG modes.

In the quantum domain (as illustrated in Fig. 1), when a pumping beam photon is annihilated in the process of parametric down conversion in the nonlinear crystal (NLC), two new twin photons are created in a process that basically follows two equiprobable decay channels: (a) both signal and idler photons are emitted in the transverse mode ψ_{HG10}; (b) both signal and idler photons are emitted in the transverse mode ψ_{HG01}. The frequencies of the interacting fields satisfy $\omega_p = \omega_s + \omega_i$, with the indexes p, s, and i indicating, respectively, pump, signal, and idler beam frequencies.

Mathematically, the fields in the OPO are described by bosonic operators $\hat{a}_i$, $i = 0,...,4$, such that

$$\begin{aligned}\psi_{00}\,\hat{\mathrm{e}}_H &\to \hat{a}_0,\\ \psi_{HG10}\,\hat{\mathrm{e}}_H &\to \hat{a}_1,\\ \psi_{HG01}\,\hat{\mathrm{e}}_H &\to \hat{a}_2,\\ \psi_{HG10}\,\hat{\mathrm{e}}_V &\to \hat{a}_3,\\ \psi_{HG01}\,\hat{\mathrm{e}}_V &\to \hat{a}_4.\end{aligned} \quad (3)$$

The intracavity fields are damped via transmittance of the mirrors and their interaction with the medium outside the OPO is described through the thermal bath operators $\hat{\Gamma}_j$, $j = 0, ..., 4$. The effective second-order nonlinearity of the crystal is denoted by χ. Therefore, in the Heisenberg picture, the Hamiltonian that describes this system is given by [31,32]

$$\hat{H} = \sum_{j=0}^{4}\hbar\omega_j\hat{a}_j^\dagger\hat{a}_j + i\hbar\chi\sum_{j=1}^{2}(\hat{a}_j^\dagger\hat{a}_{j+2}^\dagger\hat{a}_0 - \hat{a}_j\hat{a}_{j+2}\hat{a}_0^\dagger) + i\hbar\sum_{j=0}^{4}(\mathcal{E}_j e^{-i\omega_j t} - \mathcal{E}_j^* e^{i\omega_j t}) + \sum_{j=0}^{4}(\hat{a}_j\hat{\Gamma}_j^\dagger + \hat{a}_j^\dagger\hat{\Gamma}_j). \quad (4)$$

In this equation, the first term describes the number of photons inside the cavity for each mode. The second term describes the interaction between the pump beam and the signal and idler beams via the nonlinear crystal. The third

and fourth terms describe, respectively, the seed fields injected with the pumping beam and the cavity photons losses.

The complete solution of this system consists of solving the master equations for the density operator, an extremely complicated task due to the nonlinearity between the quantum operators in the Hamiltonian. Through well-known techniques in the literature to treat the thermal reservoir [33], this problem can be mapped on a Fokker-Planck equation for the probability distribution of complex amplitudes in the phase space. This equation is equivalent to the set of stochastic differential equations, in the Wigner representation [34,35], as written below:

$$\begin{aligned} d\alpha_0 &= [\mathcal{E}_0 e^{i\phi_0} - \gamma_0\alpha_0 - \chi(\alpha_1\alpha_3 + \alpha_2\alpha_4)]dt \\ &\quad + \sqrt{\gamma_0}dw_0, \\ d\alpha_1 &= (\mathcal{E}_1 e^{i\phi_1} - \gamma\alpha_1 + \chi\alpha_0\alpha_3^*)dt + \sqrt{\gamma}dw_1, \\ d\alpha_2 &= (\mathcal{E}_2 e^{i\phi_2} - \gamma\alpha_2 + \chi\alpha_0\alpha_4^*)dt + \sqrt{\gamma}dw_2, \\ d\alpha_3 &= (\mathcal{E}_3 e^{i\phi_3} - \gamma\alpha_3 + \chi\alpha_0\alpha_1^*)dt + \sqrt{\gamma}dw_3, \\ d\alpha_4 &= (\mathcal{E}_4 e^{i\phi_4} - \gamma\alpha_4 + \chi\alpha_0\alpha_2^*)dt + \sqrt{\gamma}dw_4, \end{aligned} \tag{5}$$

where α_j, with $j = 0, 1, ..., 4$, are complex amplitudes associated with the bosonic operators of the fields involved. The terms γ_0 and γ describe the losses in the cavity. Since modes 1,...,4 are degenerate in frequency, we use the same γ for the losses in all down-converted modes. The dw_j are complex Wiener processes such that

$$\langle dw_j \rangle = 0 \quad \text{and} \quad \langle dw_j dw_k^* \rangle = \delta_{jk}dt. \tag{6}$$

In order to proceed with the calculations with a direct notation, we rewrite Eq. (5) as

$$\begin{aligned} d\alpha_0 &= [\mathcal{E}_0 - \gamma_0\alpha_0 - \chi(\alpha_1\alpha_3 + \alpha_2\alpha_4)]dt + \sqrt{\gamma_0}dw_0, \\ d\alpha_j &= (\mathcal{E}_j e^{i\phi_j} - \gamma\alpha_j + \chi\alpha_0\alpha_{j+2}^*)dt + \sqrt{\gamma}dw_j, \end{aligned} \tag{7}$$

where the index j takes values $j = 1, ..., 4$ (with $\alpha_5 \equiv \alpha_1$ and $\alpha_6 \equiv \alpha_2$). Furthermore, without loss of generality, we set the pumping beam field $E_p = E_p^* = \mathcal{E}_0$ as a real-valued field by choosing $\phi_0 = 0$, so that the other fields referring to the signal and idler beams [according to Eq. (5)] have their phases defined in relation to it.

We now proceed to write the set of stochastic equations in the Langevin form, by defining complex white noises Φ_j^{in} such that [34]

$$\frac{dw_j}{dt} = \sqrt{2}\Phi_j^{in}(t), \tag{8}$$

and $\langle \Phi_j^{in}(t)\Phi_k^{in}(t') \rangle = \frac{1}{2}\delta(t - t')\delta_{jk}$. Also, we scale time as $\tau = \gamma t$ and the amplitudes as $a_0 = (\chi/\gamma)\alpha_0$ and $a_j = g\alpha_j$, with $g = \chi/\sqrt{2\gamma\gamma_0}$, to finally get the dimensionless equations

$$\begin{aligned} \frac{da_0}{d\tau} &= \gamma_r\{\mu_0 - a_0 - 2(a_1a_3 + a_2a_4) + 2g\Phi_0(\tau)\}, \\ \frac{da_j}{d\tau} &= \mu_j e^{i\phi_j} - a_j + a_0a_{j+2}^* + g\sqrt{2}\Phi_j^{in}(\tau), \end{aligned} \tag{9}$$

where $\gamma_r \equiv \gamma_0/\gamma$ and

$$\mu_0 \equiv \frac{\chi\mathcal{E}_0}{\gamma\gamma_0} \quad \text{and} \quad \mu_j \equiv \frac{\chi\mathcal{E}_j}{\gamma\sqrt{2\gamma\gamma_0}} \tag{10}$$

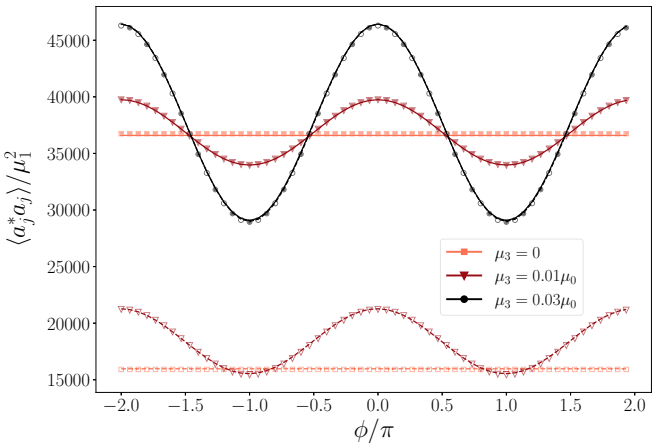

FIG. 2. Normalized steady-state output signal and idler beams as a function of the relative phase between the pump and injection beams for $\mu_0 = 0.2$. The signal injection parameter is fixed as $\mu_1 = 0.03\mu_0$, while the idler's varies from 0 to $0.03\mu_0$ (lighter to darker colors). Curves depict analytical results as in Eq. (11), while symbols depict the numerical results as in Eq. (9). Open symbols/dashed curves: idler intensity. Filled symbols/solid curves: signal intensity.

are the pump and injection parameters, respectively. When no field is injected into the optical cavity, $\mu_0 = 1$ represents the OPO's threshold for oscillation.

III. STEADY-STATE SOLUTIONS

In this section, we will investigate the classical dynamics of the system by finding the steady-state solutions of the average values of the dynamical variables. This regime is useful for the experimental analysis of the system's parameters across various phase regimes [36]. Under this condition, $da_j/dt = 0$ and the noise terms are averaged out. As a result, the system transforms into

$$\begin{aligned} \mu_0 - \bar{a}_0 - 2\sum_{j=1}^{2}\bar{a}_j\bar{a}_{j+2} &= 0, \\ \mu_j e^{i\phi_j} - \bar{a}_j + \bar{a}_0\bar{a}_{j+2}^* &= 0, \\ \mu_{j+2}e^{i\phi_{j+2}} - \bar{a}_{j+2} + \bar{a}_0\bar{a}_j^* &= 0. \end{aligned} \tag{11}$$

Rearranging the equations, it is possible to write the down-converted beam amplitudes as a function of a_0 and injection parameters μ_j:

$$\bar{a}_j = \frac{\mu_j e^{i\phi_j} + \bar{a}_0\mu_{j+2}e^{i\phi_{j+2}}}{1 - \bar{a}_0^2}, \tag{12}$$

$$\bar{a}_{j+2} = \frac{\mu_{j+2}e^{i\phi_{j+2}} + \bar{a}_0\mu_j e^{i\phi_j}}{1 - \bar{a}_0^2}. \tag{13}$$

Substituting these solutions into the initial equation from (11), one can formulate a fifth-order polynomial for a_0, which can be addressed numerically if necessary. Finally, having these solutions, we can readily determine the intensity of the converted signal and idler beams outside the cavity.

Figure 2 shows both the numerical and analytical outcomes for the steady-state intensity of the signal and idler output fields when $\mu_0 = 0.2$. These intensity profiles are plotted

against the phase $\phi = \phi_1 + \phi_3$, which represents the combined phase difference between the pump and the injected seed. It is worth noting that Eqs. (12) and (13) provide crucial insight into the system's behavior. Specifically, these equations reveal that amplitudes $\bar{a}_1$ and $\bar{a}_3$ remain entirely independent of both amplitudes $\bar{a}_2$ and $\bar{a}_4$ and phases ϕ_2 and ϕ_4. This independence indicates that the system behaves as two separate OPOs. It should be noted that the amplitudes of the pump, signal, and idler beams can be varied. When the signal and idler injection beams have equal intensities, the response observed is optimal, denoting maximum conversion. In such a scenario, the converted signal and idler exhibit identical intensities and are phase sensitive, relying on the value of the relative phase ϕ. However, if the signal injection beam is characterized by a proportionality factor of $\mu_1 = 0.03\mu_0$, while the idler injection beam has $\mu_3 = 0.01\mu_0$, the signal becomes more intense than the idler injection. Consequently, we still observe the familiar phase-sensitive phenomenon, except that the converted signal is stronger than the converted idler. In the absence of the idler injection beam, the system exhibits a distinct behavior. Specifically, we observe the generation of a relatively low-intensity idler beam, while the signal-converted beam becomes significantly stronger. In this configuration, as expected, there is no phase dependence.

IV. FIELD INTENSITIES IN THE NONDEPLETION REGIME

The set of stochastic equations (9) can be solved numerically. However, under certain conditions, these stochastic equations can be simplified and solved analytically. Here we are working with intensities of the injection beams much smaller than the intensity of the pumping beam, which, in turn, is smaller than the intensity of the OPO oscillation threshold. Under these conditions, we perform the nondepletion approach: we assume the pump beam amplitude is little affected due to the creation of photons in the down-converted modes and hence we assume a stationary regime for a_0. This means eliminating the noise Φ_0 as well as the full-time dependence of a_0 in Eq. (9). One then gets a_0 as constant and four remaining coupled equations for the modes $j = 1, \ldots, 4$,

$$\begin{aligned} a_0 &= \mu_0, \\ \frac{da_j}{d\tau} &= \mu_j e^{i\phi_j} - a_j + \mu_0 a_{j+2}^* + g\sqrt{2}\Phi_j^{in}(\tau). \end{aligned} \tag{14}$$

This approximation makes it possible to solve the system analytically, which will be done here by transforming the amplitude and noise fields to the frequency domain via Fourier transforms of the form

$$\tilde{f}(\Omega) = \frac{1}{\sqrt{2\pi}} \int_{-\infty}^{\infty} d\tau e^{-\imath\Omega\tau} f(\tau). \tag{15}$$

In summary, applying the Fourier transform to Eq. (14) and using relation (8), one gets

$$\begin{aligned} \imath\Omega\tilde{a}_j(\Omega) &= \sqrt{2\pi}\mu_j e^{i\phi_j}\delta(\Omega) - \tilde{a}_j(\Omega) \\ &\quad + \mu_0\tilde{a}_{j+2}^*(-\Omega) + g\sqrt{2}\tilde{\Phi}_j^{in}(\Omega), \\ \imath\Omega\tilde{a}_{j+2}(\Omega) &= \sqrt{2\pi}\mu_{j+2}e^{i\phi_{j+2}}\delta(\Omega) - \tilde{a}_{j+2}(\Omega) \\ &\quad + \mu_0\tilde{a}_j^*(-\Omega) + g\sqrt{2}\tilde{\Phi}_{j+2}^{in}(\Omega), \end{aligned} \tag{16}$$

which can be solved in order to give the intracavity fields

$$\begin{aligned} \tilde{a}_j(\Omega) &= \frac{\sqrt{2\pi}\mu_j e^{+i\phi_j}\delta(\Omega) + \sqrt{2\pi}\mu_{j+2}e^{-i\phi_{j+2}}\delta(\Omega)}{(1+\imath\Omega)^2 - \mu_0^2} \\ &\quad + g\sqrt{2}\frac{(1+\imath\Omega)\tilde{\Phi}_j^{in}(\Omega) + \mu_0\tilde{\Phi}_{j+2}^{*\,in}(-\Omega)}{(1+\imath\Omega)^2 - \mu_0^2}. \end{aligned} \tag{17}$$

Therefore, in this nondepletion approach, the injection and vacuum contributions for the amplitude solutions appear as two independent terms. In particular, when there is no injection ($\mu_j = \mu_{j+2} = 0$), one gets the vacuum solution

$$\tilde{a}_j^{\mathrm{VAC}}(\Omega) \equiv g\sqrt{2}\frac{(1+\imath\Omega)\tilde{\Phi}_j^{in}(\Omega) + \mu_0\tilde{\Phi}_{j+2}^{*\,in}(-\Omega)}{(1+\imath\Omega)^2 - \mu_0^2}. \tag{18}$$

Returning to the original amplitude variables, denoted as $\alpha_j = a_j/g$, we can determine the field outside the cavity through the input-output relations [33],

$$\tilde{\alpha}_j^{\mathrm{out}}(\Omega) = \sqrt{2\gamma}\tilde{\alpha}_j(\Omega) - \sqrt{\gamma}\tilde{\Phi}_j^{\mathrm{in}}(\Omega). \tag{19}$$

Therefore, substituting Eq. (17) in Eq. (19), and averaging over the ensemble, one can get the field correlations in the frequency domain, viz.,

$$\begin{aligned} &\left\langle \tilde{\alpha}_j^{*\mathrm{out}}(\Omega)\tilde{\alpha}_k^{\mathrm{out}}(\Omega')\right\rangle \\ &\quad = \delta_{jk}\delta(\Omega+\Omega')\left[\frac{1}{2} + \frac{4\gamma\mu_0^2}{\left(1-\Omega^2-\mu_0^2\right)^2 + 4\Omega^2)}\right] \\ &\qquad + 4\gamma\pi(\mu_j e^{-i\phi_j} + \mu_0\mu_{j+2}e^{+i\phi_{j+2}}) \\ &\qquad \times \frac{(\mu_k e^{i\phi_k} + \mu_0\mu_{k+2}e^{-i\phi_{k+2}})\delta(-\Omega)\delta(\Omega')}{\left(1-\Omega^2-\mu_0^2\right)^2 + 4\Omega^2} \end{aligned} \tag{20}$$

and

$$\begin{aligned} &\left\langle \tilde{\alpha}_j^{\mathrm{out}}(\Omega)\tilde{\alpha}_k^{\mathrm{out}}(\Omega')\right\rangle \\ &\quad = \gamma\left[\frac{\mu_0\left(1+\Omega^2+\mu_0^2\right)(\delta_{j,k+2}+\delta_{j+2,k})\delta(\Omega+\Omega')}{\left(1-\Omega^2-\mu_0^2\right)^2 + 4\Omega^2}\right. \\ &\qquad + 4\gamma\pi(\mu_j e^{i\phi_j} + \mu_0\mu_{j+2}e^{-i\phi_{j+2}}) \\ &\qquad \left.\times \frac{(\mu_k e^{-i\phi_k} + \mu_0\mu_{k+2}e^{-i\phi_{k+2}})\delta(\Omega)\delta(\Omega')}{\left(1-\Omega^2-\mu_0^2\right)^2 + 4\Omega^2}\right]. \end{aligned} \tag{21}$$

The intensity in each mode is obtained from Eq. (20) by setting $j = k$ and then taking an inverse Fourier transform. Figure 3(a) displays the transmitted OPO field intensity for a mode α_j, depicting its dependency on the pumping and injection parameters μ_0 and μ_j. In all analyzed situations we considered $\mu_1 = \mu_2 = \mu_3 = \mu_4 \equiv \mu$ and $\phi_2 = \phi_3 = \phi_1 = \phi_4 = 0$ such that all modes exhibit the same statistical behavior. In addition, we choose $g = 0.01$. Solid curves represent analytical results as in Eq. (20), while symbols show the results from numerical solutions of the system (9), referring to the solution of the complete set of equations without the nondepletion approximation. Numerical integrations

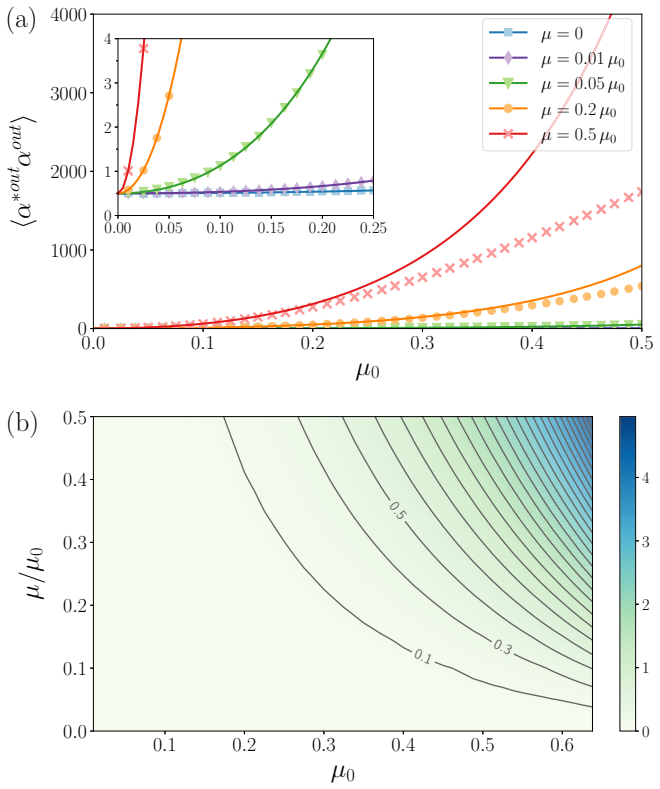

FIG. 3. (a) The intensities of the converted beams are presented as a function of the pumping beam parameter μ_0 in five different injection scenarios. Curves: analytical solution on the nondepletion regime [Eq. (20)]. Symbols: numerical integration of Eq. (9). Inset: detailed enlargement of the behavior around $\mu_0 = 0$. (b) Density plot of the relative difference ϵ between intensities in the numerical and analytical solutions [Eq. (22)]. Contour lines are spaced by 0.2 (only the first three values are shown for clarity).

of Eq. (9) were performed with a second-order predictor-corrector method [37], and both time and ensemble averages are considered after a suitable transient time.

At this point, it is important to highlight the strong agreement between the analytical and numerical curves, particularly in regimes where $\mu_0 < 0.3$ and $\mu_j < 0.2\mu_0$, as they exhibit a nearly perfect overlap. The blue curve (squares) refers to the null injection case. The inset represents a zoom in the region where the pumping parameter is less than 15% of the OPO threshold, which shows that in this regime the nondepletion approximation agrees very well with the numerical solution. As expected, in all results the intensity transmitted for $\mu_0 = 0$ is worth 0.5, bearing in mind that all mathematical developments took place in the Wigner representation where this value represents the energy of the vacuum state [33]. Figure 3(b) shows a density plot where the color intensity represents the relative distance between output intensities in the numerical and analytical solutions, namely,

$$\epsilon \equiv \frac{\left|\langle \alpha_j^{*\mathrm{out}}\alpha_j^{\mathrm{out}}\rangle_{\mathrm{num}} - \langle \alpha_j^{*\mathrm{out}}\alpha_j^{\mathrm{out}}\rangle_{\mathrm{ana}}\right|}{\langle \alpha_j^{*\mathrm{out}}\alpha_j^{\mathrm{out}}\rangle_{\mathrm{num}}}. \tag{22}$$

In the predominantly light green region, below the 0.1 contour line, one finds the typical values of μ_0 and μ in which the nondepletion approximation agrees very well with the numerical solution, such that $\epsilon < 0.1$.

V. EPR CORRELATIONS

In a more formal context, entanglement is defined by the presence of nonclassical correlations among subsystems within a quantum system. Such correlations are marked by the impossibility of representing the system's density matrix as a convex combination of factorized density matrices. This fundamental concept of separability between subsystems forms the basis for the Duan-Simon criterion, as proposed by Duan and Simon [38], which serves as a valuable tool for assessing entanglement in continuous variables. Here, we utilize the Duan-Simon criterion to detect the presence of entanglement within the beams generated by our injected OPO. To do so, we calculate the necessary spectral variances using a dual approach: analytical methods incorporating the nondepletion approximation (14), and numerical solutions for Eq. (5).

The Duan-Simon criterion [38] constitutes a mathematical inequality based on correlations between different combinations of amplitude and phase quadratures (Einstein-Podolsky-Rosen continuous variables) of the interacting modes. Therefore, in order to implement this criterion in our system, we define the quadratures

$$X_j \equiv a_j^* + a_j \quad \text{and} \quad Y_j \equiv -i(a_j^* - a_j), \tag{23}$$

which are subsequently rescaled using the following transformations:

$$\begin{aligned} x_0 &= g\sqrt{2\gamma_r}X_0, \quad y_0 = gY_0, \\ x_j &= g\sqrt{2\gamma_r}X_j, \quad y_j = gY_j. \end{aligned} \tag{24}$$

With this, Eq. (9) takes the form

$$\begin{aligned} \frac{dx_0}{d\tau} &= \gamma_r\left[2\mu_0 - x_0 - \sum_{j=1}^{2}(x_j x_{j+2} - y_j y_{j+2})\right] \\ &\quad + 2g\gamma_r\Phi_{x_0}, \\ \frac{dy_0}{d\tau} &= \gamma_r\left[-y_0 - \sum_{j=1}^{2}(x_j j_{j+2} + y_j y_{j+2})\right] \\ &\quad + 2g\gamma_r\Phi_{y_0}, \\ \frac{dx_j}{d\tau} &= 2\mu_j\cos\phi_j - x_j + \frac{1}{2}(x_0 x_{j+2} + y_0 y_{j+2}) \\ &\quad + g\sqrt{2}\Phi_{x_j}, \\ \frac{dy_j}{d\tau} &= 2\mu_j\sin\phi_j - y_j + \frac{1}{2}(x_0 y_{j+2} - y_0 x_{j+2}) \\ &\quad + g\sqrt{2}\Phi_{y_j}, \end{aligned} \tag{25}$$

where, analogously to Eq. (7), we assign $x_5 \equiv x_1$ and $x_6 \equiv x_2$ (and similarly to the y quadrature). It is worth mentioning that Eq. (25) constitute a set of coupled stochastic equations with Gaussian noise satisfying [34]

$$\begin{aligned} \langle \Phi_{x_i}(\tau)\rangle &= \langle \Phi y_i(\tau)\rangle = 0 \\ \langle \Phi_{x_i}(\tau)\Phi_{x_j}(\tau')\rangle &= \langle \Phi_{y_i}(\tau)\Phi_{y_j}(\tau')\rangle = \delta_{ij}\delta(\tau - \tau'). \end{aligned} \tag{26}$$

The occurrence of quadrature quantum correlations become evident by defining new quadratures that encompass both the signal and idler modes, namely,

$$x^{+}_{j,j+2} = \frac{x_j + x_{j+2}}{\sqrt{2}}, \quad x^{-}_{j,j+2} = \frac{x_j - x_{j+2}}{\sqrt{2}},$$
$$y^{-}_{j,j+2} = \frac{y_j - y_{j+2}}{\sqrt{2}}, \quad y^{+}_{j,j+2} = \frac{y_j + y_{j+2}}{\sqrt{2}}. \tag{27}$$

In these new variables, the equations with nondepletion approximation of the pump beam read

$$\begin{aligned}
\frac{dx^{+}_{j,j+2}}{d\tau} &= (2\mu_j \cos\phi_j + 2\mu_{j+2}\cos\phi_{j+2}) - (1-\mu_0)x^{+}_{j,j+2} \\
&\quad + g\sqrt{2}(\Phi_{x_j} + \Phi_{x_{j+2}}), \\
\frac{dy^{+}_{j,j+2}}{d\tau} &= (2\mu_j \sin\phi_j + 2\mu_{j+2}\sin\phi_{j+2}) - (1+\mu_0)y^{+}_{j,j+2} \\
&\quad + g\sqrt{2}(\Phi_{y_j} + \Phi_{y_{j+2}}), \\
\frac{dx^{-}_{j,j+2}}{d\tau} &= (2\mu_j \cos\phi_j - 2\mu_{j+2}\cos\phi_{j+2}) - (1+\mu_0)x^{-}_{j,j+2} \\
&\quad + g\sqrt{2}(\Phi_{x_j} - \Phi_{x_{j+2}}), \\
\frac{dy^{-}_{j,j+2}}{d\tau} &= (2\mu_j \sin\phi_j - 2\mu_{j+2}\sin\phi_{j+2}) - (1-\mu_0)y^{-}_{j,j+2} \\
&\quad + g\sqrt{2}(\Phi_{y_j} - \Phi_{y_{j+2}}).
\end{aligned} \tag{28}$$

Interestingly, this change of variables decouples the set of equations in terms of the variables representing the combined quadratures. Nevertheless, Eq. (28) still entail correlations via the noise terms that are combined in the process, causing the suppression of quantum fluctuations (squeezing) in a pair of quadratures, at the cost of increasing fluctuations (antisqueezing) in the remaining pair, all according to the Heisenberg uncertainty principle.

Therefore, in order to verify the squeezing and antisqueezing situations, we calculated the correlation spectra associated with the combinations of the four quadratures of interest. We will proceed from here with calculations in the frequency domain since from an experimental point of view it is the quantity easily accessed outside the cavity.

Applying a Fourier transform to Eq. (28), we get

$$\begin{aligned}
\tilde{x}^{+}_{j,j+2}(\Omega) &= \frac{1}{1-\mu_0+i\Omega}\big\{2\sqrt{\pi}\delta(\Omega)(\mu_j\cos\phi_j \\
&\quad + \mu_{j+2}\cos\phi_{j+2}) + g\sqrt{2}\big[\tilde{\Phi}_{x_j}(\Omega) + \tilde{\Phi}_{x_{j+2}}(\Omega)\big]\big\}, \\
\tilde{y}^{+}_{j,j+2}(\Omega) &= \frac{1}{1+\mu_0+i\Omega}\big\{2\sqrt{\pi}\delta(\Omega)(\mu_j\sin\phi_j \\
&\quad + \mu_{j+2}\sin\phi_{j+2}) + g\sqrt{2}\big[\tilde{\Phi}_{y_j}(\Omega) + \tilde{\Phi}_{y_{j+2}}(\Omega)\big]\big\}, \\
\tilde{x}^{-}_{j,j+2}(\Omega) &= \frac{1}{1+\mu_0+i\Omega}\big\{2\sqrt{\pi}\delta(\Omega)(\mu_j\cos\phi_j \\
&\quad - \mu_{j+2}\cos\phi_{j+2}) + g\sqrt{2}\big[\tilde{\Phi}_{x_j}(\Omega) - \tilde{\Phi}_{x_{j+2}}(\Omega)\big]\big\}, \\
\tilde{y}^{-}_{j,j+2}(\Omega) &= \frac{1}{1-\mu_0+i\Omega}\big\{2\sqrt{\pi}\delta(\Omega)(\mu_j\sin\phi_j \\
&\quad - \mu_{j+2}\sin\phi_{j+2}) + g\sqrt{2}\big[\tilde{\Phi}_{y_j}(\Omega) - \tilde{\Phi}_{y_{j+2}}(\Omega)\big\},
\end{aligned} \tag{29}$$

where the noise terms, now in Fourier space, must obey

$$\begin{aligned}
\big\langle\tilde{\Phi}_{m_j}(\Omega)\big\rangle &= 0, \\
\big\langle\tilde{\Phi}_{m_j}(\Omega)\tilde{\Phi}_{m_k}(\Omega')\big\rangle &= \delta_{jk}\delta(\Omega+\Omega').
\end{aligned} \tag{30}$$

Once more applying the input-output relation Eq. (19), we derive the expressions for the correlations beyond of the cavity (extracavity).

$$\begin{aligned}
\langle\tilde{y}^{+}_{j,j+2}\tilde{y}^{+*}_{j,j+2}\rangle_{\text{out}} &= \delta(\Omega+\Omega')\left[1 - \frac{4\mu_0}{(1+\mu_0)^2+\Omega^2}\right] + 8\gamma\pi\delta(\Omega)\delta(\Omega')\frac{(\mu_j\sin\phi_j + \mu_{j+2}\sin\phi_{j+2})^2}{(1+\mu_0)^2+\Omega^2}, \\
\langle\tilde{x}^{-}_{j,j+2}\tilde{x}^{-*}_{j,j+2}\rangle_{\text{out}} &= \delta(\Omega+\Omega')\left[1 - \frac{4\mu_0}{(1+\mu_0)^2+\Omega^2}\right] + 8\gamma\pi\delta(\Omega)\delta(\Omega')\frac{(\mu_j\cos\phi_j - \mu_{j+2}\cos\phi_{j+2})^2}{(1+\mu_0)^2+\Omega^2}, \\
\langle\tilde{y}^{-}_{j,j+2}\tilde{y}^{-*}_{j,j+2}\rangle_{\text{out}} &= \delta(\Omega+\Omega')\left[1 + \frac{4\mu_0}{(1-\mu_0)^2+\Omega^2}\right] + 8\gamma\pi\delta(\Omega)\delta(\Omega')\frac{(\mu_j\sin\phi_j - \mu_{j+2}\sin\phi_{j+2})^2}{(1-\mu_0)^2+\Omega^2}, \\
\langle\tilde{x}^{+}_{j,j+2}\tilde{x}^{+*}_{j,j+2}\rangle_{\text{out}} &= \delta(\Omega+\Omega')\left[1 + \frac{4\mu_0}{(1-\mu_0)^2+\Omega^2}\right] + 8\gamma\pi\delta(\Omega)\delta(\Omega')\frac{(\mu_j\cos\phi_j + \mu_{j+2}\cos\phi_{j+2})^2}{(1-\mu_0)^2+\Omega^2}.
\end{aligned} \tag{31}$$

It is noticeable that the injection terms solely impact the zero-frequency component of the correlation spectra. Away from this frequency, one may identify the light noise spectrum with the expressions of the averages of the combined quadratures provided by Eq. (31) as in

$$\begin{aligned}
&V^{m_{k,k+2}}_{n_{l,l+2}}(\Omega)\delta(\Omega+\Omega') \\
&\quad = \langle\Delta m_{k,k+2}(\Omega)\Delta n_{l,l+2}(\Omega')\rangle,
\end{aligned} \tag{32}$$

where m, n refer to any of the combined quadratures $x^{\pm}$ or $y^{\pm}$ and $\Delta m_{j,j+2}(\Omega) \equiv m_{j,j+2}(\Omega) - \langle m_{j,j+2}(\Omega)\rangle$. Here, $V^{m_{k,k+2}}_{n_{l,l+2}}(\Omega)$ is the extracavity noise spectrum of light. Formally, when $m = n$ and $k = l$, we get

$$\begin{aligned}
&\langle\Delta m_{k,k+2}(\Omega)\Delta m_{k,k+2}(\Omega')\rangle = 1 \Rightarrow \text{shot noise}, \\
&\langle\Delta m_{k,k+2}(\Omega)\Delta m_{k,k+2}(\Omega')\rangle < 1 \Rightarrow \text{squeezing}, \\
&\langle\Delta m_{k,k+2}(\Omega)\Delta m_{k,k+2}(\Omega')\rangle > 1 \Rightarrow \text{antisqueezeing}.
\end{aligned}$$

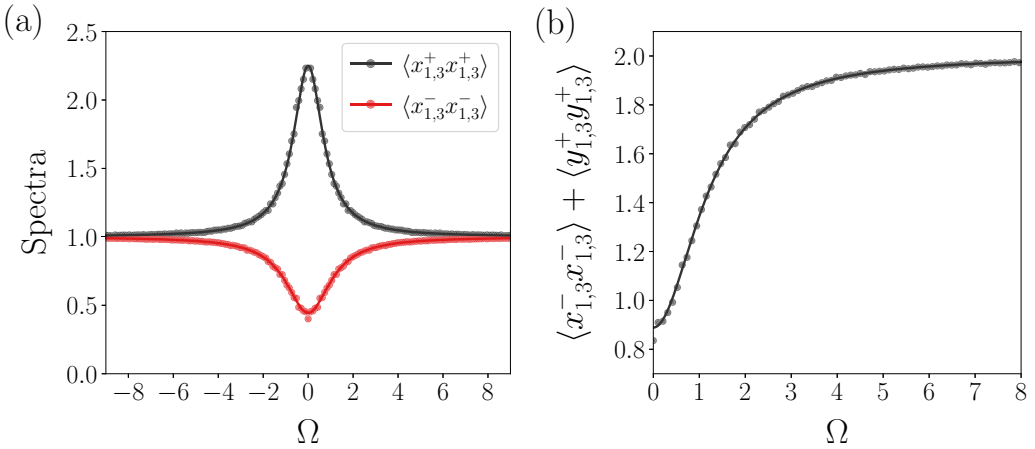

FIG. 4. (a) Noise spectrum for squeezing and antisqueezing quadratures when $\mu_0 = 0.2$, $\mu_j = 0.01\mu_0$ and $\phi_j = 0$. (b) Duan-Simon spectrum. Points: numerical simulations. Lines: analytical results with nondepletion approximation, Eq. (31).

By the Duan-Simon criterion, there is entanglement if the inequality

$$\langle \Delta m_{k,k+2}(\Omega)^2\rangle + \langle \Delta n_{l,l+2}(\Omega)^2\rangle \geqslant 2 \tag{33}$$

is violated, which happens when we select pairs of quadratures that are simultaneously squeezed, that is, EPR pairs such as $\{x^-_{k,k+2}, y^+_{k,k+2}\}$ and $\{x^+_{k,k+2}, y^-_{k,k+2}\}$.

Figure 4 provides an overview of the correlation spectra and the Duan-Simon criterion for the system, with $\mu_0 = 0.2$ and $\mu_j = 0.01\mu_0$. Both plots display the results of numerical simulations for the complete equations (points), as well as the analytical solutions in the nondepletion regime (solid lines). Figure 4(a) showcases both the squeezed $\langle x_- x_-\rangle$ and the antisqueezed $\langle x_+ x_+\rangle$ spectra, while Fig. 4(b) presents the Duan-Simon spectrum. Notably, the spectrum curve consistently remains below 2 (thus violating the Duan-Simon condition), with its minimum value occurring around $\Omega = 0$. We should mention that the zero-frequency components obtained with the numerical solutions lie outside the plot scale, as expected due to the presence of the delta functions in Eq. (31). Generally, it is observed that the spectra curves of the system without seed injection closely resemble the case illustrated in Fig. 4. This observation suggests that the injection of a seed can effectively drive the oscillating modes while preserving the entanglement.

VI. DISCRETE VARIABLES BELL INEQUALITY VIOLATION

In this section, we propose an experiment that aims to verify the violation of Bell's inequality using discrete variables instead of continuous variables obtained elsewhere [26]. The advantage here is that we do not need to use homodyne measurement on the output fields, which proves to be a difficult task. In the present case, verifying the violation of Bell's inequality to test the theory of local realism seems to be more viable through the use of less sophisticated measuring devices. Specifically, Bell-type quantum correlations can be verified and quantified using the scheme illustrated in Fig. 5. In this scheme, S is a source that emits pairs of linearly polarized photons in the horizontal (H) and vertical (V) directions in the first-order Hermite-Gauss modes HG_{01} and HG_{10}, which are sent to two observers: Alice (A) and Bob (B). The source S illustrated in the diagram internally separates the photons based on their polarization. Consequently, photons polarized as H are sent to Alice, while those polarized as V are sent to Bob. Therefore, each pair emitted by the source is described by a state of four modes: A_h, A_v B_h, and B_v, in which the indices h and v refer to the modes HG_{10} horizontal and HG_{01} vertical, respectively. Alice and Bob can mix their respective modes using appropriate optical elements C to subsequently perform measurements $\{\theta_A, \theta'_A\}$ and $\{\theta_B, \theta'_B\}$ referring to $\hat{A}^+$, $\hat{A}^-$, $\hat{B}^+$, and $\hat{B}^-$ modes. Alice and Bob can perform single photon measurements resulting in $R \in \{0, 1\}$ at each detector. Repeating this procedure, they can build the joint statistics of correlations between them, given by

$$R^{ij}(\theta_A, \theta_B) = \left\langle R^i_A(\theta_A) R^j_B(\theta_B)\right\rangle, \tag{34}$$

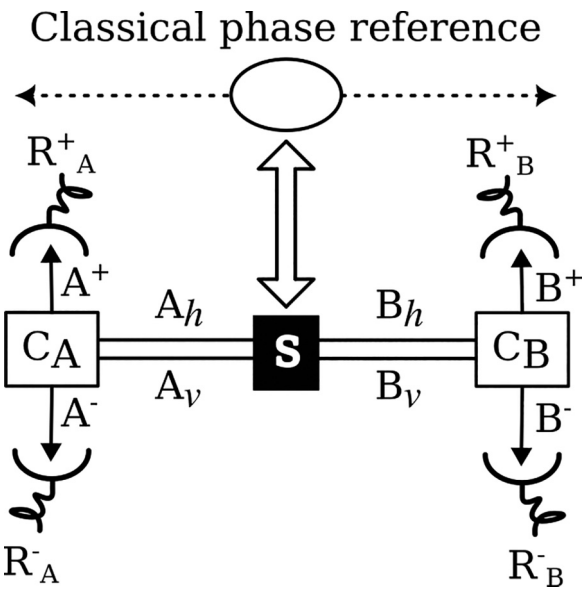

FIG. 5. A diagram for a Bell test.

where $i, j \in \{+, -\}$. We can construct a function based on the four possible combinations, as outlined in [26]

$$E(\theta_A, \theta_B) = \frac{M}{N}, \tag{35}$$

where

$$\begin{aligned} M = & R^{++}(\theta_A, \theta_B) + R^{--}(\theta_A, \theta_B) \\ & - R^{+-}(\theta_A, \theta_B) - R^{-+}(\theta_A, \theta_B), \end{aligned} \tag{36}$$

and N is a normalization term given by

$$\begin{aligned} N = & R^{++}(\theta_A, \theta_B) + R^{--}(\theta_A, \theta_B) \\ & + R^{+-}(\theta_A, \theta_B) + R^{-+}(\theta_A, \theta_B), \end{aligned} \tag{37}$$

that is, the sum of all possible outcomes.

The quantity $E(\theta_A, \theta_B)$ accounts for the expectation values for each set of measures. These expectation values can be used in the construction of the Clauser-Horne-Shimony-Holt (CHSH) inequality

$$B = |E(\theta_A, \theta_B) + E(\theta'_A, \theta'_B) + E(\theta'_A, \theta_B) - E(\theta_A, \theta'_B)| \leqslant 2, \tag{38}$$

an inequality that determines the range of possible outcomes according to local realism but that can be violated if applied to entangled states. The maximum violation occurs when the experimental setup angles are $\theta_A = \{\pi/8, 3\pi/8\}$ and $\theta_B = \{0, \pi/4\}$.

The correlation represented in Eq. (34) can be constructed by continuous variables with amplitudes in positive-P representation, based on normal ordering, as

$$R_N^{ij} = \langle \hat{A}_i^\dagger(\theta_A)\hat{A}_i(\theta_A)\hat{B}_j^\dagger(\theta_B)\hat{B}_j(\theta_B)\rangle. \tag{39}$$

However, using the Wigner representation, based on symmetric ordering, Eq. (39) can be mapped into

$$\begin{aligned} R_S^{ij} = & \langle [\hat{A}_i^\dagger(\theta_A)\hat{A}_i(\theta_A) - \langle \hat{A}_i^\dagger(\theta_A)\hat{A}_i(\theta_A)\rangle]. \\ & \times [\hat{B}_j^\dagger(\theta_B)\hat{B}_j(\theta_B) - \langle \hat{B}_j^\dagger(\theta_B)\hat{B}_j(\theta_B)\rangle]\rangle, \end{aligned} \tag{40}$$

where the averages of the intensities were subtracted in the calculation of the correlation function. As one of our main results, we compute below the CHSH inequality in both representations.

The transformations applied by the elements C_A and C_B, which modify the modes within the Alice and Bob frames, can be expressed as follows:

$$\begin{aligned} A_+ &= \cos(\theta_A)a_1 + \sin(\theta_A)a_2, \\ A_- &= \sin(\theta_A)a_1 - \cos(\theta_A)a_2, \\ B_+ &= \cos(\theta_B)a_3 + \sin(\theta_B)a_4, \\ B_- &= \sin(\theta_B)a_3 - \cos(\theta_B)a_4, \end{aligned} \tag{41}$$

where the amplitudes a_i are associated with the seeded fields from Eq. (3). Now, using these amplitudes, we proceed by computing Eq. (35) in both normal and symmetrical orderings. It can be demonstrated that both Eq. (39) and (40) yield identical numerators, namely,

$$\begin{aligned} M(\alpha, \beta) = & \cos(2\alpha)\cos(2\beta)E_1 + \cos(2\alpha)\sin(2\beta)E_2 \\ & + \sin(2\alpha)\cos(2\beta)E_3 - \sin(2\alpha)\sin(2\beta)E_4, \end{aligned} \tag{42}$$

with

$$\begin{aligned} E_1 = & \langle a_1^* a_1 a_3^* a_3\rangle + \langle a_2^* a_2 a_4^* a_4\rangle \\ & - \langle a_1^* a_1 a_4^* a_4\rangle - \langle a_2^* a_2 a_3^* a_3\rangle \\ & + (\langle a_1^* a_1\rangle - \langle a_2^* a_2\rangle) * (\langle a_4^* a_4\rangle - \langle a_3^* a_3\rangle), \\ E_2 = & \langle a_1^* a_1 a_3^* a_4\rangle + \langle a_1^* a_1 a_4^* a_3\rangle \\ & - \langle a_2^* a_2 a_3^* a_4\rangle - \langle a_2^* a_2 a_4^* a_3\rangle, \\ E_3 = & \langle a_1^* a_2 a_3^* a_3\rangle + \langle a_2^* a_1 a_3^* a_3\rangle \\ & - \langle a_1^* a_2 a_3^* a_4\rangle - \langle a_2^* a_1 a_4^* a_4\rangle, \\ E_4 = & \langle a_1^* a_1 a_3^* a_3\rangle + \langle a_2^* a_2 a_4^* a_4\rangle \\ & - \langle a_1^* a_1 a_4^* a_4\rangle - \langle a_2^* a_2 a_3^* a_3\rangle \\ & + (\langle a_3^* a_4\rangle - \langle a_4^* a_3\rangle) * (\langle a_1^* a_2\rangle - \langle a_2^* a_1\rangle). \end{aligned} \tag{43}$$

For further calculations, we assume we are dealing with Gaussian variables, whose higher-order correlations reduce to combinations of second-order ones, as

$$\langle abcd\rangle = \langle ab\rangle\langle cd\rangle + \langle ac\rangle\langle bd\rangle + \langle ad\rangle\langle bc\rangle - 2\langle a\rangle\langle b\rangle\langle c\rangle\langle d\rangle. \tag{44}$$

The normalization process [Eq. (37)] produces remarkably diverse outcomes depending on the representation one employs. Specifically, in the case of symmetrical ordering, it becomes

$$\begin{aligned} N_S = & \langle a_1^* a_1 a_3^* a_3\rangle + \langle a_1^* a_1 a_4^* a_4\rangle \\ & + \langle a_2^* a_2 a_3^* a_3\rangle + \langle a_2^* a_2 a_3^* a_3\rangle, \end{aligned} \tag{45}$$

while in normal ordering

$$N_N = N_S - 1 - [\langle a_1^* a_1\rangle + \langle a_2^* a_2\rangle + \langle a_3^* a_3\rangle + \langle a_4^* a_4\rangle]. \tag{46}$$

Incorporating all the previously obtained results into Eq. (37), we generate a graph depicting the Bell parameter B against frequency.

In summary, we show in Fig. (6) the function B defined in (38) on the Wigner (dashed lines) and positive-P (solid lines) representations for three different injection scenarios, corresponding to $\mu_j = 0$, $\mu_j = 0.01\mu_0$, and $\mu_j = 0.03\mu_0$ (from lighter to darker colors). Once again, symbols represent numerical solutions and lines the analytical result with nondepletion approximation. In the null injection case, one observes the Bell inequality violation up to $\mu_0 \approx 0.4$ on the positive-P case.

As envisioned and discussed in Ref. [39], it is important to note that the violation of the Bell inequality depends on the ordering of quantum operators; it can be violated under normal ordering (positive-P representation) but is not violated under symmetric ordering (Wigner representation). This discussion can be deepened in the classical domain considering the Cauchy-Schwartz inequality [40], where the authors have shown that the violation occurs only in the normal ordering of the operators. On can summarize

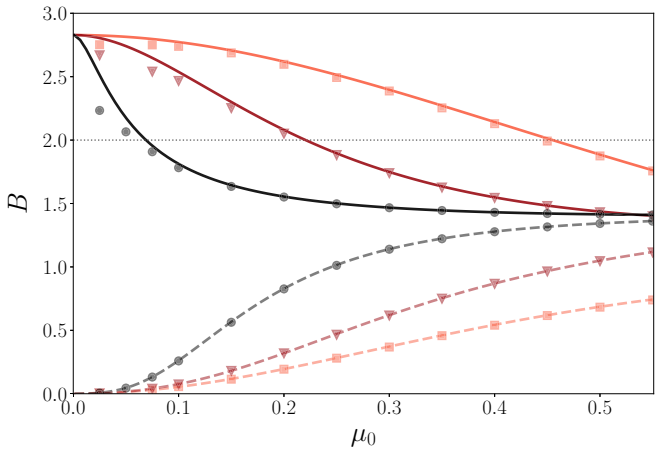

FIG. 6. Verification of the CHSH inequality through computation of function B from Eq. (38), shown here as a function of the pump intensity. The three different injection regimes depicted correspond to $\mu_j = 0$, $\mu_j = 0.01\mu_0$, and $\mu_j = 0.03\mu_0$ (lighter to darker colors). Symbols: numerical simulations. Solid: positive-P representation. Dashed: Wigner representation.

these results in two cases: experimental setups based only on homodyne detection are described in symmetric ordering, where background vacuum is also measured, leading to no violation of Bell-type inequalities; experimental setups based on direct intensity measures are described in normal ordering, which can violate the Bell inequalities [41].

Here, when $\mu_j = 0.01\mu_0$, one observes again a violation but in a smaller region, up to $\mu_0 \approx 0.2$. It is also noted that in the case where $\mu_j = 0.03\mu_0$, one has an even smaller violation region, indicating that the injection degrades the entanglement. We observe that the slight mismatch between numerical and analytical results seen for small μ_0 is not due to any significantly different behavior, but only to a slow statistical convergence of numerical results in this regime, as we could observe by comparing many distinct realizations.

Finally, in Fig. 7 we show the schematic diagram of the experimental proposal for observing the violation of Bell inequalities in the injected OPO. The theory described in Sec. II relies on a simultaneous resonance of the converted (and injected) fields in the OPO cavity. It is important to point out that this condition is not trivially achieved, since astigmatic effects, coming from the nonlinear crystal birefringence, may prevent this situation [22]. It is important to mention that the injected seed beams are necessary to drive the OPO operation with the required spatial modes. Otherwise, if the OPO is left with the pump input alone, the fundamental Gaussian mode, which has a lower oscillation threshold, will take over and dominate the device operation. The seed beams allow for spatial mode control while adding an acceptable amount of noise. In practice, a two-crystal setup can be used to overcome this issue [20]. In this proposal, initially, the pumping beam is separated from the converted beams by means of a dichroic mirror (DM). The converted beams are then split on a polarizing beam splitter (PBS) and distributed to Alice and Bob. Alice receives the horizontally polarized beams and Bob the vertically polarized ones. Alice and Bob have Dove prisms

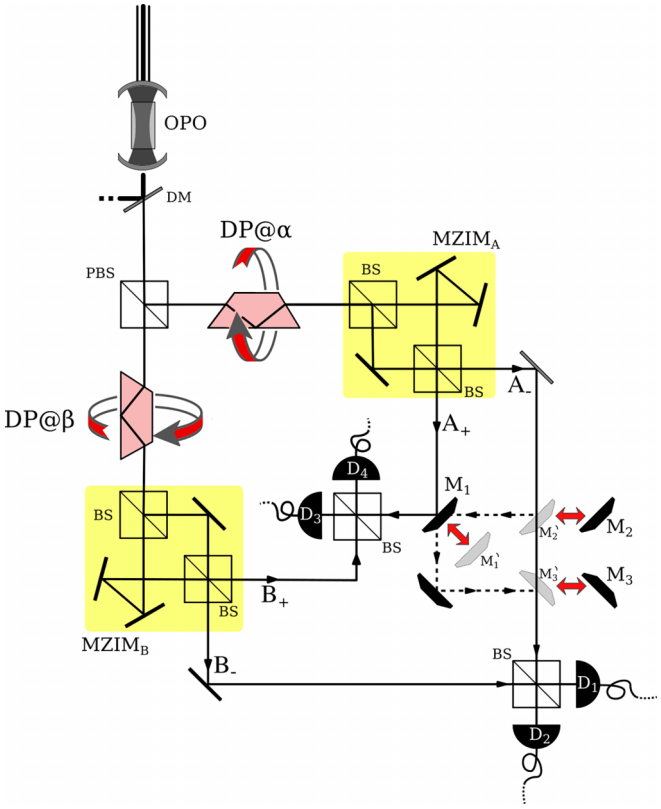

FIG. 7. An experimental proposal to measure Bell correlations in entangled beams generated by an injected OPO.

that perform the mixtures $C_{A,B}$, according to the diagram depicted in Fig. 5. Two Mach-Zehnder interferometers with additional mirrors, often referred to as MZIM as introduced by Ref. [42], separate the incoming fields of the Alice and Bob in A_+, A_-, B_+, and B_-, which are mapped on Eq. (41). Subsequently, these signals are mixed and detected on two arrays with beam splitters and photodetectors. An articulated assemble can move the mirrors M_1, M_2, and M_3 to positions M_1', M_2', and M_3', respectively, enabling the exchange between the fields A_+ and A_- so that on can obtain all the correlations $\langle A_+B_+\rangle$, $\langle A_-B_+\rangle$, $\langle A_+B_-\rangle$, and $\langle A_-B_-\rangle$. The photocurrents generated by the photodetectors are used so as to obtain the needed correlations indicated in Eq. (43).

VII. CONCLUSION

In summary, this study demonstrates the efficacy of injecting a signal into the lower-frequency first-order spin-orbit modes of the nondegenerate optical parametric oscillator for the generation of nonclassical states of light. Our findings reveal that this technique successfully amplifies the intensity of low-frequency modes below the standard oscillation threshold while preserving quantum correlations. We have derived and solved stochastic equations to describe the system's dynamics, both analytically and numerically, under stationary and dynamic nondepletion conditions. This analysis validates the compatibility between analytical and numerical nondepletion results. To assess entanglement, we calculated quantum correlations between the beams' quadratures and employed them to

construct the Duan-Simon criterion and CHSH inequalities, the latter serving as a tool to observe Bell's inequalities within the system. Conclusively, we propose an experimental setup utilizing a weakly injected OPO for Bell's inequalities measurement based on coincidences measurements. Our findings highlight the system's capability to generate spin-orbit hyperentangled states, establishing it as a valuable resource for applications in quantum technology and fundamental physics.

ACKNOWLEDGMENTS

Funding was provided by Coordenação de Aperfeiçoamento de Pessoal de Nível Superior (CAPES), Fundação Carlos Chagas Filho de Amparo à Pesquisa do Estado do Rio de Janeiro (FAPERJ), and Instituto Nacional de Ciência e Tecnologia de Informação Quântica (INCT-IQ 465469/2014-0). A.Z.K. acknowledges financial support from Fundação de Amparo à Pesquisa do Estado de São Paulo (Grant No. 2021/06823-5).

[1] E. Schrödinger, Die gegenwärtige situation in der quantenmechanik, Naturwissenschaften **23**, 844 (1935).

[2] A. Einstein, B. Podolsky, and N. Rosen, Can quantum-mechanical description of physical reality be considered complete? Phys. Rev. **47**, 777 (1935).

[3] J. S. Bell, On the Einstein Podolsky Rosen paradox, Phys. Phys. Fiz. **1**, 195 (1964).

[4] F. Flamini, N. Spagnolo, and F. Sciarrino, Photonic quantum information processing: A review, Rep. Prog. Phys. **82**, 016001 (2019).

[5] A. Aspect, P. Grangier, and G. Roger, Experimental tests of realistic local theories via Bell's theorem, Phys. Rev. Lett. **47**, 460 (1981).

[6] A. Aspect, P. Grangier, and G. Roger, Experimental realization of Einstein-Podolsky-Rosen-Bohm *gedankenexperiment:* A new violation of Bell's inequalities, Phys. Rev. Lett. **49**, 91 (1982).

[7] C. H. Bennett and G. Brassard, Quantum cryptography: Public key distribution and coin tossing, Theor. Comput. Sci. **560**, 7 (2014).

[8] P. W. Shor, Polynomial-time algorithms for prime factorization and discrete logarithms on a quantum computer, SIAM J. Comput. **26**, 1484 (1997).

[9] S. Lloyd, Universal quantum simulators, Science **273**, 1073 (1996).

[10] S. L. Braunstein and P. van Loock, Quantum information with continuous variables, Rev. Mod. Phys. **77**, 513 (2005).

[11] W. P. Bowen, N. Treps, B. C. Buchler, R. Schnabel, T. C. Ralph, H.-A. Bachor, T. Symul, and P. K. Lam, Experimental investigation of continuous-variable quantum teleportation, Phys. Rev. A **67**, 032302 (2003).

[12] A. M. Lance, T. Symul, W. P. Bowen, B. C. Sanders, and P. K. Lam, Tripartite quantum state sharing, Phys. Rev. Lett. **92**, 177903 (2004).

[13] N. Treps, N. Grosse, W. P. Bowen, C. Fabre, H.-A. Bachor, and P. K. Lam, A quantum laser pointer, Science **301**, 940 (2003).

[14] J. Aasi, J. Abadie, B. P. Abbott, R. Abbott, T. D. Abbott, M. R. Abernathy, C. Adams, T. Adams, P. Addesso, R. X. Adhikari *et al.*, Enhanced sensitivity of the LIGO gravitational wave detector by using squeezed states of light, Nat. Photonics **7**, 613 (2013).

[15] N. C. Menicucci, S. T. Flammia, and O. Pfister, One-way quantum computing in the optical frequency comb, Phys. Rev. Lett. **101**, 130501 (2008).

[16] A. S. Coelho, F. A. S. Barbosa, K. N. Cassemiro, A. S. Villar, M. Martinelli, and P. Nussenzveig, Three-color entanglement, Science **326**, 823 (2009).

[17] A. Montaña Guerrero, R. L. Rincón Celis, P. Nussenzveig, M. Martinelli, A. M. Marino, and H. M. Florez, Continuous variable entanglement in an optical parametric oscillator based on a nondegenerate four wave mixing process in hot alkali atoms, Phys. Rev. Lett. **129**, 163601 (2022).

[18] N. Takanashi, W. Inokuchi, T. Serikawa, and A. Furusawa, Generation and measurement of a squeezed vacuum up to 100 MHz at 1550 nm with a semi-monolithic optical parametric oscillator designed towards direct coupling with waveguide modules, Opt. Express **27**, 18900 (2019).

[19] B. C. dos Santos, K. Dechoum, and A. Z. Khoury, Continuous-variable hyperentanglement in a parametric oscillator with orbital angular momentum, Phys. Rev. Lett. **103**, 230503 (2009).

[20] K. Liu, J. Guo, C. Cai, S. Guo, and J. Gao, Experimental generation of continuous-variable hyperentanglement in an optical parametric oscillator, Phys. Rev. Lett. **113**, 170501 (2014).

[21] R. Rodrigues, J. Gonzales, B. P. da Silva, J. Huguenin, M. Martinelli, R. M. de Araújo, C. Souza, and A. Khoury, Orbital angular momentum symmetry in a driven optical parametric oscillator, Opt. Lett. **43**, 2486 (2018).

[22] M. Martinelli, J. A. O. Huguenin, P. Nussenzveig, and A. Z. Khoury, Orbital angular momentum exchange in an optical parametric oscillator, Phys. Rev. A **70**, 013812 (2004).

[23] G. B. Alves, R. F. Barros, D. S. Tasca, C. E. R. Souza, and A. Z. Khoury, Conditions for optical parametric oscillation with a structured light pump, Phys. Rev. A **98**, 063825 (2018).

[24] T. C. Ralph, W. J. Munro, and R. E. S. Polkinghorne, Proposal for the measurement of Bell-type correlations from continuous variables, Phys. Rev. Lett. **85**, 2035 (2000).

[25] E. H. Huntington and T. C. Ralph, Continuous-variable Bell-type correlations from two bright squeezed beams, Phys. Rev. A **65**, 012306 (2001).

[26] O. Thearle, J. Janousek, S. Armstrong, S. Hosseini, M. Schünemann (Mraz), S. Assad, T. Symul, M. R. James, E. Huntington, T. C. Ralph, and P. K. Lam, Violation of Bell's inequality using continuous variable measurements, Phys. Rev. Lett. **120**, 040406 (2018).

[27] C. E. R. Souza, J. A. O. Huguenin, P. Milman, and A. Z. Khoury, Topological phase for spin-orbit transformations on a laser beam, Phys. Rev. Lett. **99**, 160401 (2007).

[28] C. V. S. Borges, M. Hor-Meyll, J. A. O. Huguenin, and A. Z. Khoury, Bell-like inequality for the spin-orbit separability of a laser beam, Phys. Rev. A **82**, 033833 (2010).

[29] K. H. Kagalwala, G. Di Giuseppe, A. F. Abouraddy, and B. E. A. Saleh, Bell's measure in classical optical coherence, Nat. Photonics **7**, 72 (2013).

[30] M. J. Padgett and J. Courtial, Poincaré-sphere equivalent for light beams containing orbital angular momentum, Opt. Lett. **24**, 430 (1999).

[31] M. D. Reid and P. D. Drummond, Correlations in nondegenerate parametric oscillation: Squeezing in the presence of phase diffusion, Phys. Rev. A **40**, 4493 (1989).

[32] R. Graham and H. Haken, The quantum-fluctuations of the optical parametric oscillator. I, Z. Phys. A: Hadrons Nucl. **210**, 276 (1968).

[33] D. Walls and G. J. Milburn, *Quantum Optics* (Springer, New York, 2008).

[34] K. Dechoum, P. D. Drummond, S. Chaturvedi, and M. D. Reid, Critical fluctuations and entanglement in the nondegenerate parametric oscillator, Phys. Rev. A **70**, 053807 (2004).

[35] B. C. dos Santos, K. Dechoum, A. Z. Khoury, L. F. da Silva, and M. K. Olsen, Quantum analysis of the nondegenerate optical parametric oscillator with injected signal, Phys. Rev. A **72**, 033820 (2005).

[36] N. Wang and Y. Li, Quantum analysis and experimental investigation of the nondegenerate optical parametric oscillator with unequally injected signal and idler, Phys. Rev. A **93**, 013831 (2016).

[37] P. E. Kloeden and E. Platen, *Numerical Solution of Stochastic Differential Equations* (Springer, Berlin, 1992).

[38] L.-M. Duan, G. Giedke, J. I. Cirac, and P. Zoller, Inseparability criterion for continuous variable systems, Phys. Rev. Lett. **84**, 2722 (2000).

[39] H. M. Faria, K. Dechoum, and A. Z. Khoury, Bell inequality violation and operator ordering in quantum theory, Phys. Rev. A **102**, 053714 (2020).

[40] L. F. da Silva, A. Z. Khoury, and K. Dechoum, Entanglement criteria and classical correlations in parametric amplifiers, Phys. Rev. A **78**, 025803 (2008).

[41] B. Stiller, U. Seyfarth, and G. Leuchs, Temporal and spectral properties of quantum light, arXiv:1411.3765.

[42] H. Sasada and M. Okamoto, Transverse-mode beam splitter of a light beam and its application to quantum cryptography, Phys. Rev. A **68**, 012323 (2003).